Journal of Advanced Ceramics
2016, **5**(3): 244–252
DOI: 10.1007/s40145-016-0196-y

ISSN 2226-4108
CN 10-1154/TQ

Research Article

$Ce_{1-x}Sm_xO_{2-x/2}$—A novel type of ceramic material for thermal barrier coatings

Xiao-ge CHEN[a], Haoming ZHANG[b], Hong-song ZHANG[b,c,*], Yong-de ZHAO[c], Gang LI[b]

[a]*Department of Construction Engineering, Henan Institute of Engineering, Zhengzhou 450007, China*
[b]*Department of Mechanical Engineering, Henan Institute of Engineering, Zhengzhou 450007, China*
[c]*Institute of Chemistry Henan Academy Sciences, Zhengzhou 450052, China*

Received: April 09, 2016; Revised: June 09, 2016; Accepted: June 11, 2016

Abstract: In this study, $Ce_{1-x}Sm_xO_{2-x/2}$ ceramics were synthesized by sol–gel route and solid state sintering method. The phase structure was analyzed by X-ray diffraction (XRD), Fourier transform infrared (FTIR) spectroscopy, and Raman spectroscopy. The morphologies of the synthesized powders and the corresponding bulk samples were observed using scanning electron microscopy (SEM). Their thermal diffusivities and thermal expansion coefficients were measured by the laser-flash method and the pushing-rod method, respectively. Results show that pure $Ce_{1-x}Sm_xO_{2-x/2}$ powders with single fluorite structure are synthesized successfully, and their microstructures of the corresponding bulk samples are very dense. With the increase of Sm_2O_3 content, their thermal expansion coefficients decrease due to the higher electro-negativity of Sm^{3+} ions as compared with that of Ce^{4+} ions. Their thermal conductivities at 1000 ℃ lie in the range of 1.62–2.02 W/(m·K) due to the phonon scattering caused by the substituted atoms and oxygen vacancies. The $Ce_{1-x}Sm_xO_{2-x/2}$ ceramics can be used as ceramic candidates for novel thermal barrier coatings (TBCs).

Keywords: thermal barrier coatings (TBCs); CeO_2 oxides; doping; thermophyscial properties

1 Introduction

Thermal barrier coatings (TBCs) are advanced material system which is always used to protect underlying metallic components in turbine engines from damage caused by corrosive hot gas or high temperature [1–3]. In the system of thermal barrier coatings, the ceramic top coat shields the underlying material from heat, and the metallic bond protects the substrate against high temperature degradation and improves adherence of the top coat [4]. Because of the excellent thermophysical properties, 7–8 wt% yttria-stabilized zirconia (YSZ) ceramic has been widely employed as the top coat material by the current commercial thermal barrier coatings in high temperature turbine components. However, the thermal insulation ability and working lifetime of the YSZ thermal barrier coating can be injured severely for long-term application above 1200 ℃ due to its inherent phase transformation and enhanced sintering [5,6]. Therefore, it is very urgent to develop alternatives to YSZ for advanced TBC applications.

The excellent ceramic candidates for TBCs must possess a few important performances, such as low thermal conductivity, appropriate thermal expansion,

* Corresponding author.
E-mail: zhs761128@163.com

good phase stability at high temperature, low sintering rate, high melting point, chemical inertness, and good adherence to the metal substrate [7]. However, ceramic materials matching all the requirements are still very rare in light of the current standard. Now, low thermal conductivity and appropriate thermal expansion coefficient have been regarded as the primary selection criterions of the ceramic materials for TBC applications. In recent years, ceramic oxides with pyrochlore structure or defect fluorite structure have been widely studied [8–11]. Except for the $A_2B_2O_7$-type (A = rare earth element, B = Zr, Ce, Hf, Sn) oxides [1–10], the cerium oxides with fluorite structure have recently attracted extensive attention due to a diversity of applications, such as conversion catalysts for selective hydrogenation of unsatured compounds, catalysts for three-way automobile exhaust systems, abrasives for chemical polishing slurries, gates for metal-oxide semiconductor devices, and luminescent materials for violet/blue fluorescence [12–14]. Now, the rare earth doped CeO_2 (RE_2O_3–CeO_2) have also been considered to be new materials for TBCs and solid oxide fuel cells due to the excellent electrical, mechanical, and thermophysical properties [15–17]. For example, Cao *et al*. [18] studied the thermal conductivity and thermal expansion coefficient of $La_2Ce_2O_7$. Patwe *et al*. [19] reported the lattice thermal expansion of $Gd_2Ce_xZr_{2-x}O_7$. Zhang *et al.* investigated the thermophysical properties of $(Sm_{1-x}Gd_x)_2Ce_2O_7$ [20] and $(Sm_{1-x}Dy_x)_2Ce_2O_7$ [21]. Zha *et al.* [22] found that the electrical conductivities of $Ce_{1-x}Gd_xO_{2-x/2}$ (GDC) and $Ce_{1-x}Sm_xO_{2-x/2}$ (SDC) at 700 ℃ are almost equal to the value of YSZ at 1000 ℃. Compared with pure doped ceria oxide (DCO) electrolyte, the DCO–chloride or DCO–carbonate composite electrolyte not only has much higher ionic conductivity, but also shows higher ionic transference number at intermediate temperature range [23,24], and these electrolytes also have good chemical stability [25].

Although thermophysical properties of a few rare earth stabilized CeO_2 have been reported by some researchers, the present reports about rare earth stabilized CeO_2 applications for TBCs are still not systemic. Therefore, investigation of the thermophysical properties of rare earth stabilized CeO_2 is still of notable significance. Previous works have discussed the electrical conductivity of $Ce_{1-x}Sm_xO_{2-x/2}$ system, but did not deal with thermophysical properties of $Ce_{1-x}Sm_xO_{2-x/2}$ oxides. In the present study, $Ce_{1-x}Sm_xO_{2-x/2}$ oxides were synthesized by sol–gel method and pressureless sintering technology, and the phase composition and thermophysical properties of $Ce_{1-x}Sm_xO_{2-x/2}$ ($x = 0.1$, 0.3, and 0.5) oxides were evaluated.

2 Experiment

In the current investigation, Sm_2O_3 powders (Rare-Chem Hi-Tech Co. Ltd., Guangdong, China; purity ≥ 99.9%) and $Ce(NO_3)\cdot 6H_2O$ (Zibo Huantuo Chemical Co. Ltd.; analytical pure) were chosen as the raw materials. Before weighting the raw powders, the samarium oxide powders were firstly calcined at 800 ℃ for 2 h to remove the adsorptive water and carbon dioxide in air, and then weighted samarium oxide powders were dissolved in diluting nitric acid. $Ce(NO_3)\cdot 6H_2O$ was dissolved in distilled water and all solutions were mixed with constant stirring. Subsequently, the pH value of the mixed solution was adjusted to 6 by adding ammonia hydroxide drop wise. At the same time, ethylene glycol was put into the resultant solution, and the mole ratio of ethylene glycol to cerium was 1.8:1. The mixed solution was then continuously evaporated on a water bath till a viscous liquid was obtained, and the viscous liquid was heated at 130 ℃ using air oven till a porous solid mass was obtained. The obtained porous solid mass was ground in an agate mortar and activated at 800 ℃ for 2 h in a muffle oven. At the end, the achieved powders were isostatically cold pressed into pellets at 100 MPa, and the pellets were pressureless sintered at 1600 ℃ for 10 h in air to fabricate dense bulk samples.

An X-ray diffractometer (XRD, D8advance Bruker) with Ni filtered Cu Kα radiation (0.1542 nm) was used to analyze the phase structure of the synthesized powders and the corresponding bulk samples. The infrared spectra and Raman patterns of the synthesized powders were recorded by a Fourier transform infrared (FTIR) spectrometer (Nicolet 380) and a laser Raman spectrometer (Renishaw inVia-Reflex), respectively. A scanning electron microscope (SEM, Quanta-250, FEI) was selected to observe the microstructure of the synthesized powders and the corresponding bulk samples.

A high temperature dilatometer (Model Netzsch DIL 402C/7, Germany) was utilized to measure the thermal expansion coefficients (TECs) of bulk samples in the temperature range of 20–1200 ℃. The thermal diffusivity measurement (λ) in 200–1000 ℃ was

carried out using laser-flash method (Model LFA1000, Linseis, Germany) in an argon atmosphere. The specific heat capacity (c_p) from 20 to 1200 ℃ was calculated using Neumann–Kopp rule in light of the reference specific heat values of Sm_2O_3 and CeO_2 [26]. The actual bulk density (ρ) of the sintered samples was measured by the Archimedes drainage method at room temperature. The thermal conductivity (k) of $Ce_{1-x}Sm_xO_{2-x/2}$ oxides was achieved by Eq. (1), and the actual thermal conductivity (k_0) was computed using Eq. (2) [21] in order to eliminate the influence of porosity (ϕ) on thermal conductivity of bulk samples.

$$k = \lambda \cdot \rho \cdot c_p \tag{1}$$

$$k = \left(1 - \frac{4}{3}\phi\right)k_0 \tag{2}$$

3 Results and discussion

3. 1 Characterization about powders

The X-ray diffraction patterns of the synthesized powders are displayed in Fig. 1 together with the data of CeO_2. Clearly, the X-ray diffraction patterns of $Ce_{1-x}Sm_xO_{2-x/2}$ powders are consistent with that of CeO_2, which means that pure $Ce_{1-x}Sm_xO_{2-x/2}$ powders with single fluorite structure are synthesized successfully in the current study. The diffraction peaks near 28.51°, 33.01°, 47.17°, and 55.88° can be indexed to the (111), (200), (220), and (311) planes of fluorite structure, respectively. With the increase of Sm_2O_3 content, the X-ray diffraction peaks corresponding to the (111), (200), and (220) planes shift gradually to the lower angles, which also implies that the Sm^{3+} ions have entered the crystal lattice of CeO_2, and this result can also be confirmed by the increasing crystal lattice parameters displayed in Fig. 2. From Fig. 1, the peak width of $Ce_{0.9}Sm_{0.1}O_{1.95}$ is greater than those of $Ce_{0.7}Sm_{0.3}O_{1.85}$ and $Ce_{0.5}Sm_{0.5}O_{1.75}$, which signifies that $Ce_{0.9}Sm_{0.1}O_{1.95}$ has a small particle size as compared to those of $Ce_{0.7}Sm_{0.3}O_{1.85}$ and $Ce_{0.5}Sm_{0.5}O_{1.75}$. In addition, several weak peaks in the XRD pattern of $Sm_{0.5}Ce_{0.5}O_{1.75}$ near 30° and 32° can also be found, which can be attributed to the tiny amount un-dissolved Sm_2O_3 in the procedure of sol–gel synthesis.

Figure 3 reveals the FTIR spectra of $Ce_{1-x}Sm_xO_{2-x/2}$ powders calcined at 800 ℃ for 2 h in the wave number range of 500–4000 cm^{-1}. Obviously, several typical infrared absorption bands can be found at about

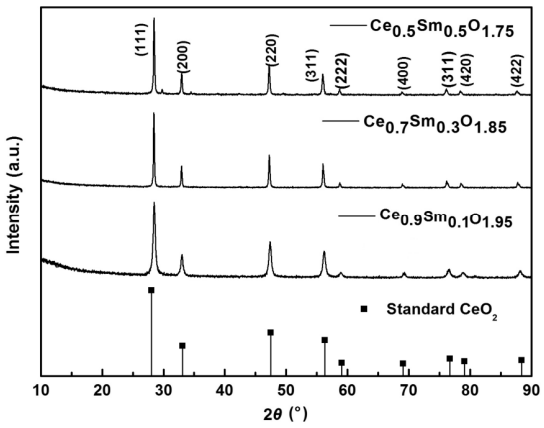

Fig. 1 XRD patterns of the synthesized $Ce_{1-x}Sm_xO_{2-x/2}$ powders.

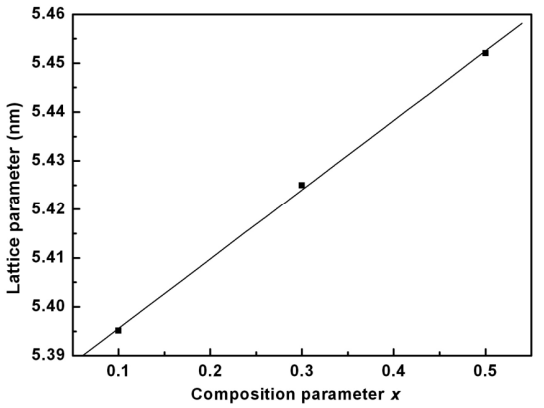

Fig. 2 Relationship between lattice parameter and doping content in $Ce_{1-x}Sm_xO_{2-x/2}$ system.

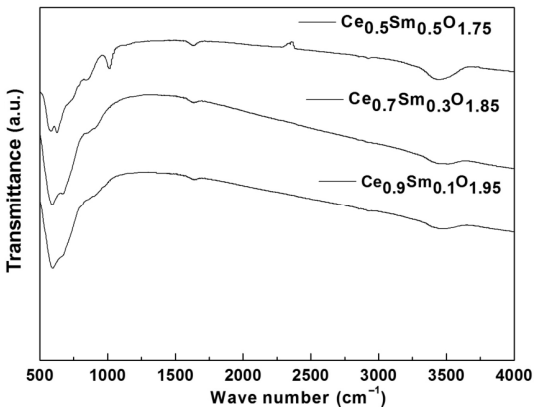

Fig. 3 FTIR spectra of $Ce_{1-x}Sm_xO_{2-x/2}$ powders.

570–590, 620–680, 1620–1640, and 3400–3500 cm^{-1}. Another absorption band at about 1010 cm^{-1} can be observed in FTIR pattern of $Ce_{0.5}Sm_{0.5}O_{1.75}$, which can be attributed to the little residual Sm_2O_3 powders [27]. The absorption band near the 3400–3500 cm^{-1} is the evidence of water molecules contained in the powders [28], and the band located at 1620–1640 cm^{-1}

represents another vibration of the water molecules [29]. The bands near 570–590 and 620–680 cm^{-1} are the typical absorption peaks of CeO_2, and the variation of intensity and wave number of these two infrared bands can be attributed to the doping of Sm_2O_3 [30].

The typical Raman patterns of $Ce_{1-x}Sm_xO_{2-x/2}$ powders are plotted in Fig. 4 together with the data of micron-size CeO_2. In the case of micron-size CeO_2, the main peak at 461.49 cm^{-1} can be attributed to the F_{2g} Raman band from the space group *Fm*3*m* of cubic fluorite structure [31,32]. With the increasing content of Sm_2O_3, the width of the main Raman band enhances clearly, which means that a large number of oxygen vacancies are created [31,33]. Furthermore, the main peak of $Ce_{0.5}Sm_{0.5}O_{1.75}$ obviously shifts to higher position compared to those of $Ce_{0.9}Sm_{0.1}O_{1.95}$ and $Ce_{0.7}Sm_{0.3}O_{1.85}$, which can be attributed to the small distortions of the atomic positions caused by Sm_2O_3 doping [34]. In the Raman spectra of $Ce_{0.7}Sm_{0.3}O_{1.85}$ and $Ce_{0.5}Sm_{0.5}O_{1.75}$, a small shoulder at 600 cm^{-1} can be assigned as a longitudinal optical mode arising due to the relaxation of symmetry rules [35], and the additional low intensity Raman bands around 250.65 and 375.22 cm^{-1} are usually assigned to the presence of extrinsic oxygen vacancies generated into the ceria lattice improving diffusion rate of bulk oxygen after samarium addition [36].

The micro-morphology of the $Ce_{1-x}Sm_xO_{2-x/2}$ powders is displayed in Fig. 5. Obviously, the synthesized $Ce_{1-x}Sm_xO_{2-x/2}$ powders exhibit a certain agglomeration. $Ce_{0.7}Sm_{0.3}O_{1.85}$ and $Ce_{0.5}Sm_{0.5}O_{1.75}$ have a size of about 50 nm; however, the average particle size of $Ce_{0.9}Sm_{0.1}O_{1.95}$ is only about 15 nm. The average particle size obtained from SEM is consistent with the analytical results of XRD.

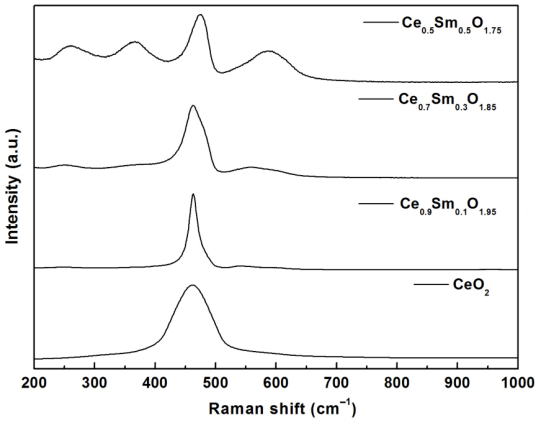

Fig. 4 Raman patterns of $Ce_{1-x}Sm_xO_{2-x/2}$ powders.

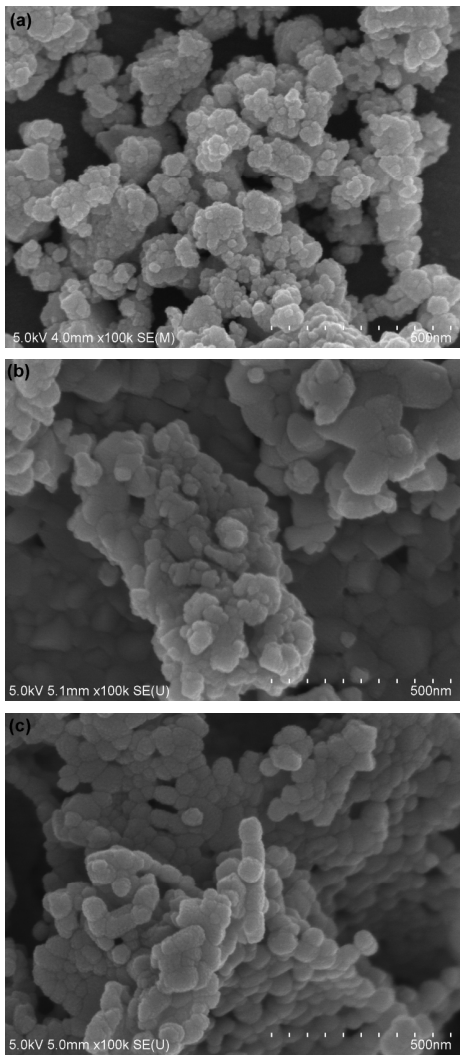

Fig. 5 Micro-morphology of $Ce_{1-x}Sm_xO_{2-x/2}$ powders: (a) $x = 0.1$, (b) $x = 0.3$, (c) $x = 0.5$.

3. 2 Characterization of bulk samples

The XRD patterns of the sintered $Ce_{1-x}Sm_xO_{2-x/2}$ samples are plotted in Fig. 6. Obviously, the X-ray diffraction patterns for bulk samples are very close to those displayed in Fig. 1, which means that the densified samples still remain the single fluorite structure. From Fig. 6, the weak peaks near 30° and 32° in the XRD pattern of $Ce_{0.5}Sm_{0.5}O_{1.75}$ disappear, which means that the residual Sm_2O_3 also enters the lattice of CeO_2 in the procedure of sintering. It can be observed clearly from Fig. 7 that the grain size of these bulk ceramics is inhomogenous, and the average grain size is several micrometers. The obtained bulk samples have dense microstructure; however, some apparent pores can still be seen in Fig. 7. Their relative densities determined by actual density and theoretical density in sequence are 93.7%, 92.8%, and 95.6%; the grain

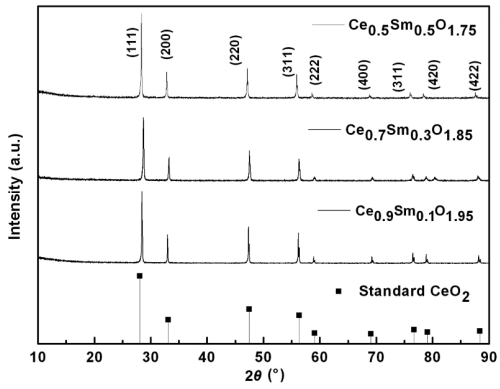

Fig. 6 XRD patterns of the $Ce_{1-x}Sm_xO_{2-x/2}$ bulk samples.

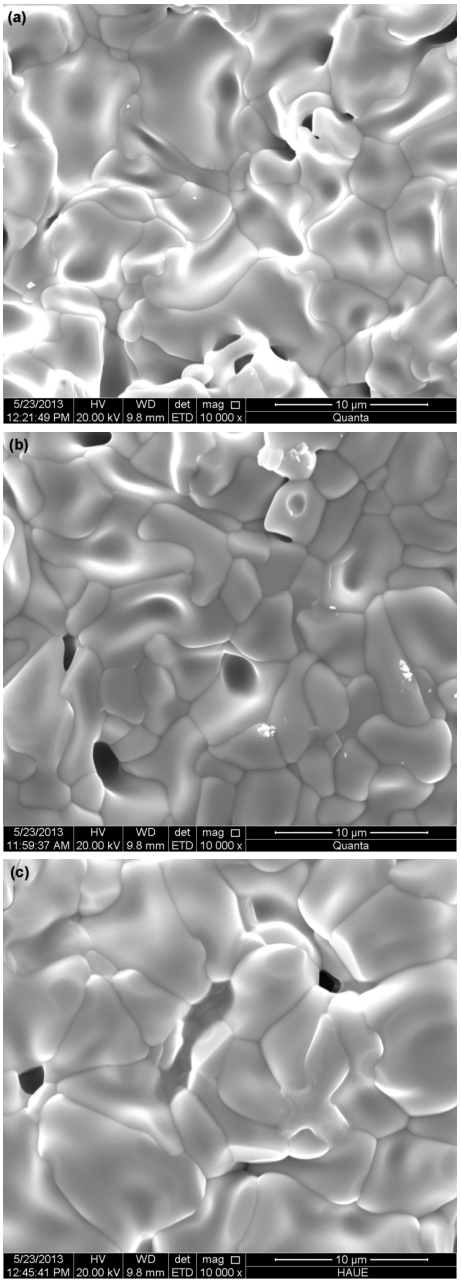

Fig. 7 Microstructure of the sintered $Ce_{1-x}Sm_xO_{2-x/2}$ samples: (a) $x = 0.1$, (b) $x = 0.3$, (c) $x = 0.5$.

boundaries are very clean and no other phases can be found in these interfaces.

3.3 Thermal expansion coefficients

The dilatometric measurement data of $Ce_{1-x}Sm_xO_{2-x/2}$ ceramics with calibration are presented in Fig. 8. Clearly, the typical linear thermal expansion property can be noted in the measuring temperature range of 20–1200 ℃, which also means that there is no phase transformation occurred in the measuring temperature range. In order to minimize the mismatch between the ceramic layer and the metal substrate, a high thermal expansion coefficient for ceramics of TBCs is required. The temperature dependence of the thermal expansion coefficient of $Ce_{1-x}Sm_xO_{2-x/2}$ ceramics is exhibited in Fig. 9, together with the data of 8YSZ which were measured in the former research of the authors. As shown in Fig. 9, the thermal expansion shows an increasing temperature tendency owing to the increasing atomic spacing at high temperatures. From Fig. 9, the thermal expansion coefficient of $Ce_{1-x}Sm_xO_{2-x/2}$ decreases gradually with increasing Sm_2O_3 content, and $Ce_{0.5}Sm_{0.5}O_{1.75}$ has the lowest thermal expansion coefficient, which is still higher than that of 8YSZ. It is well known that the thermal expansion has close relationship with the ionic bond strength, and the ionic bond strength is affected by the electro-negativity of cations composing the crystal expressed as the following equation [37]:

$$I_{\text{A-B}} = 1 - \mathrm{e}^{\frac{-(x_{\text{A}} - x_{\text{B}})}{4}} \tag{3}$$

where $I_{\text{A-B}}$ represents the ionic bond strength between ions at A site and B site, and x_{A} and x_{B} are electro-negativity of ions at A site and B site respectively. For CeO_2, the ions at sites A and B are

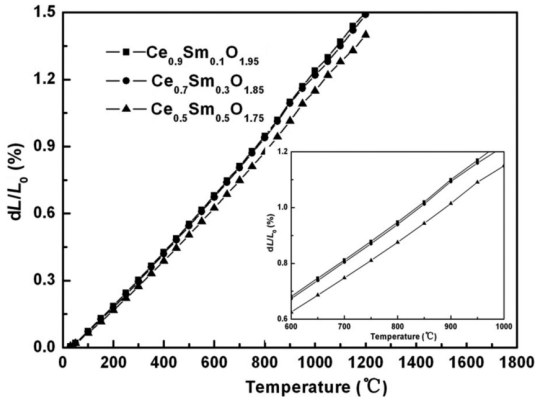

Fig. 8 Thermal expansion rate of $Ce_{1-x}Sm_xO_{2-x/2}$ ceramics at different temperature.

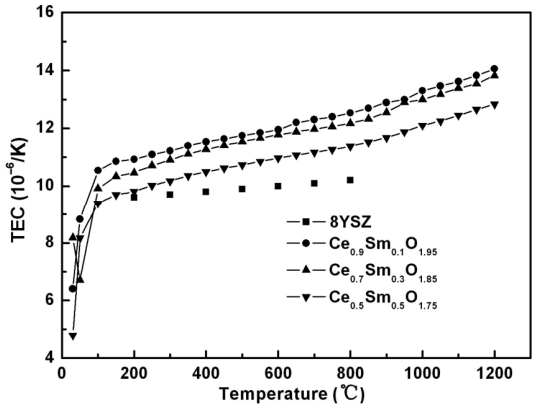

Fig. 9 Thermal expansion coefficient of $Ce_{1-x}Sm_xO_{2-x/2}$ as a function of temperature.

Ce^{4+} and O^{2-}, respectively; partial substitution of Sm^{3+} for Ce^{4+} can increase the electro-negativity of cations at A sites owning to the higher electro-negativity of Sm^{3+} ions (1.17) compared with that of Ce^{4+} ions (1.12). Therefore, it can be concluded that the thermal expansion coefficient of $Ce_{1-x}Sm_xO_{2-x/2}$ ceramics decreases with increasing Sm_2O_3 content. However, the thermal expansion coefficients of $Ce_{1-x}Sm_xO_{2-x/2}$ ceramics are still higher than that of 8YSZ, which still fulfills the basic requirement for thermal barrier coatings.

3. 4 Thermal conductivity

Based on the specific heat values of CeO_2 and Sm_2O_3, the computed specific heat capacities of $Ce_{1-x}Sm_xO_{2-x/2}$ ceramics according to the Neumann–Kopp rule are plotted in Fig. 10. Obviously, the specific heat capacity of $Ce_{1-x}Sm_xO_{2-x/2}$ ceramics increases with the increasing temperature, and decreases with Sm_2O_3 content at identical temperatures.

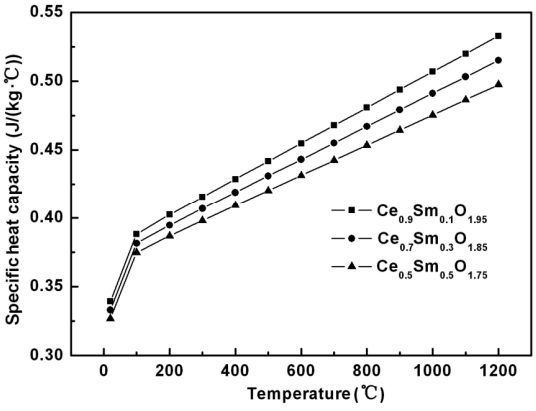

Fig. 10 Specific heat capacity of $Ce_{1-x}Sm_xO_{2-x/2}$ as a function of temperature.

The dependence of thermal diffusivity of $Ce_{1-x}Sm_xO_{2-x/2}$ ceramics on temperature is shown in Fig. 11, and the data displayed in Fig. 11 are average values of every three measurements at identical temperature. It can be observed clearly that the thermal diffusivities decrease gradually with increasing temperature in the present measuring temperature range, which shows a typical phonon thermal conduction mechanism.

In light of the values of thermal diffusivity, density, and specific heat capacity of $Ce_{1-x}Sm_xO_{2-x/2}$ ceramics, the final values of thermal conductivity are plotted in Fig. 12. It can be noted that the thermal conductivity is inversely proportional to the increasing temperature in the current temperature range, and the thermal conductivities of $Ce_{1-x}Sm_xO_{2-x/2}$ ceramics decrease obviously with the increase of Sm_2O_3 content. However, the thermal conductivity of $Ce_{0.5}Sm_{0.5}O_{1.75}$ is slightly higher than that of $Ce_{0.7}Sm_{0.3}O_{1.85}$. According to the phonon thermal conduction theory, the thermal conductivity in electrical insulation solids is proportional to the mean free path of phonon. The

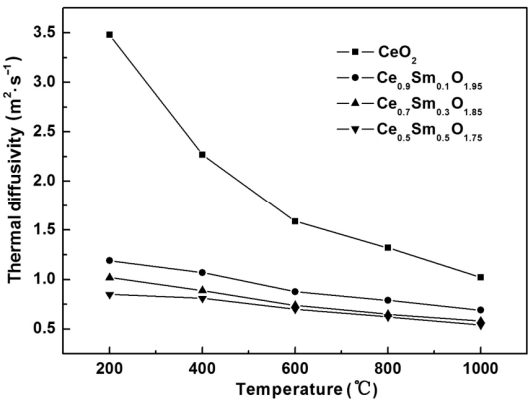

Fig. 11 Thermal diffusivity of $Ce_{1-x}Sm_xO_{2-x/2}$ ceramics.

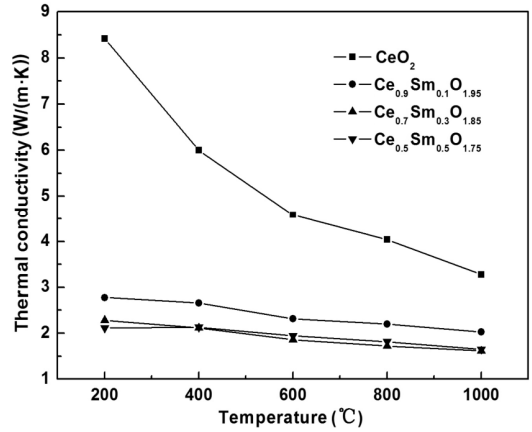

Fig. 12 Temperature dependence of thermal conductivity of $Ce_{1-x}Sm_xO_{2-x/2}$ ceramics.

phonon mean free path can be reduced when they interact with lattice defects existed in actual crystal lattice, and the influence of lattice defects including vacancies, dislocations, grain boundaries, and substituting atoms, on phonon mean free path can be expressed as

$$\frac{1}{l(\omega,T)}=\frac{1}{l_{\mathrm{i}}(\omega,T)}+\frac{1}{l_{\mathrm{p}}(\omega,t)}+\frac{1}{l_{\mathrm{v}}(\omega,T)}+\frac{1}{l_{\mathrm{gb}}} \quad (4)$$

where $\frac{1}{l_{\mathrm{i}}(\omega,T)}$, $\frac{1}{l_{\mathrm{p}}(\omega,T)}$, $\frac{1}{l_{\mathrm{v}}(\omega,T)}$, and $\frac{1}{l_{\mathrm{gb}}}$ represent the phonon mean free paths due to interstitial scattering, point defect scattering, vacancy scattering, and grain boundary scattering, respectively [38]. Because only the nanometer grain boundary can result in significant influence on phonon mean free path, so the influence of grain boundary can be ignored according to the microstructure plotted in Fig. 7 [39]. Thus, only point defects can result in obvious influence on the phonon mean free path. In crystal lattice of $Ce_{1-x}Sm_xO_{2-x/2}$ ceramics, there exist two types of point defects, including oxygen vacancies and substituting atoms, due to the substitution of Sm^{3+} cation for Ce^{4+} cation. On one hand, the oxygen vacancies can increase the effective phonon scattering and decrease the phonon mean free path. On the other hand, the differences of atomic mass and ionic radius between Sm^{3+} and Ce^{4+} can also decrease the phonon mean free path in light of Eq. (5) and Eq. (6) [21], which contributes to the lower thermal conductivity of $Ce_{1-x}Sm_xO_{2-x/2}$ ceramics.

$$\frac{1}{\overline{l}}=\frac{2ca^3\omega^4}{\pi v^4}J^2\gamma^2\left(\frac{\Delta R}{R}\right)^2 \quad (5)$$

$$\frac{1}{l_{\mathrm{p}}}=\frac{ca^3\omega^4}{4\pi v^4}\left(\frac{\Delta M}{M}\right)^2 \quad (6)$$

where a^3 is the volume of each atom, v the transverse wave speed, ω the phonon frequency, c the concentration per atom, J the constant, γ the Grüneisen parameter, M and R the average atomic mass and ionic radius of the host atom respectively, ΔM and ΔR the difference of mass and ionic radius between the substituting and the substituted cations respectively. Thus, doping of Sm_2O_3 oxide clearly reduces the thermal conductivities of the $Ce_{1-x}Sm_xO_{2-x/2}$ ceramics. The slightly higher thermal conductivity of $Ce_{0.5}Sm_{0.5}O_{1.75}$ as compared to that of $Ce_{0.7}Sm_{0.3}O_{1.85}$, can be attributed to the formation of oxygen vacancy pairs, which means the reduction of effective-oxygen number in the $Ce_{0.5}Sm_{0.5}O_{1.75}$ crystal lattice [40,41]. The thermal conductivities of $Ce_{1-x}Sm_xO_{2-x/2}$ ceramics are in the range of 1.62–2.02 W/(m·K) at 1000 ℃, which are clearly lower than that of dense 7.0 wt% YSZ (3.0 at room temperature to 2.3 W/(m·K) at 700 ℃ reported by Wu *et al.* [8]). Therefore, the synthesized $Ce_{1-x}Sm_xO_{2-x/2}$ ceramics are promising candidate materials for future thermal barrier coatings.

4 Conclusions

(1) Pure fluorite-type $Ce_{1-x}Sm_xO_{2-x/2}$ powders and the corresponding dense bulk ceramics were prepared successfully by sol–gel route and pressureless sintering method, respectively. The synthesized powders exhibit a certain agglomeration, and the bulk samples have dense microstructure whose relative densities are greater than 90%.

(2) Because of the higher electro-negativity of Sm^{3+} ions as compared to that of Ce^{4+} ions, the thermal expansion coefficients of $Ce_{1-x}Sm_xO_{2-x/2}$ ceramics decrease gradually with the increasing Sm_2O_3 content. Their thermal expansion coefficients are higher than that of 8YSZ, which still fulfills the basic requirement of thermal barrier coatings.

(3) The thermal conductivities of the $Ce_{1-x}Sm_xO_{2-x/2}$ ceramics lie in the range of 1.62–2.02 W/(m·K) at 1000 ℃, which are obviously lower than that of 7.0 wt% YSZ. The lower thermal conductivities can mainly be attributed to the phonon scattering caused by substituted atoms and oxygen vacancies in $Ce_{1-x}Sm_xO_{2-x/2}$ crystal lattice.

(4) The excellent thermophysical properties indicate that the $Ce_{1-x}Sm_xO_{2-x/2}$ ceramics are promising candidates for the next generation thermal barrier coatings.

Acknowledgements

The authors would like to thank the financial support from the National Natural Science Foundation of China (No. U1304512), the Scientific and Technological Projects of Henan Province (No. 132102210142), the Program for Science & Technology Innovation Talents in Universities of Henan Province (No. 13HASTIT018), and the Postaldoctoral Research Sponsorship in Henan Province (No. 2014069).

References

[1] Slámečka K, Čelko L, Skalka P, *et al*. Bending fatigue failure of atmospheric-plasma-sprayed CoNiCrAlY + YSZ thermal barrier coatings. *Int J Fatigue* 2015, **70**: 186–195.

[2] Bobzin K, Zhao LD, Öte M, *et al*. Deposition and characterization of thermal barrier coatings of ZrO_2–4mol.% Y_2O_3–1 mol.% Gd_2O_3–1 mol.% Yb_2O_3. *Surf Coat Technol* 2015, **268**: 205–208.

[3] Liu Z-G, Zhang W-H, Ouyang J-H, *et al*. Novel thermal barrier coatings based on rare-earth zirconates/YSZ double-ceramic-layer system deposited by plasma spraying. *J Alloys Compd* 2015, **647**: 438–444.

[4] Wang Y, Bai Y, Yang QZ, *et al*. A transmission electron microscopy study of the microstructure and interface of zirconia-based thermal barrier coatings. *J Alloys Compd* 2015, **619**: 820–825.

[5] Eriksson R, Johansson S, Brodin H, *et al*. Influence of substrate material on the life of atmospheric plasma sprayed thermal barrier coatings. *Surf Coat Technol* 2013, **232**: 795–803.

[6] Zhao PF, Sun CA, Zhu XY, *et al*. Fracture toughness measurements of plasma-sprayed thermal barrier coatings using a modified four-point bending method. *Surf Coat Technol* 2010, **204**: 4066–4074.

[7] Wang C, Wang Y. Thermophysical properties of $La_2(Zr_{0.7}Ce_{0.3})_2O_7$ prepared by hydrothermal synthesis for nano-sized thermal barrier coatings. *Ceram Int* 2015, **41**: 4601–4607.

[8] Wu J, Wei X, Padture NP, *et al*. Low-thermal-conductivity rare-earth zirconates for potential thermal-barrier-coating applications. *J Am Ceram Soc* 2002, **85**: 3031–3035.

[9] Wan C, Qu Z, He Y, *et al*. Ultralow thermal conductivity in highly anion-defective aluminates. *Phys Rev Lett* 2008, **101**: 085901.

[10] Rai AK, Schmitt MP, Bhattacharya RS, *et al*. Thermal conductivity and stability of multilayered thermal barrier coatings under high temperature annealing conditions. *J Eur Ceram Soc* 2015, **35**: 1605–1612.

[11] Feng J, Xiao B, Zhou R, *et al*. Anisotropic elastic and thermal properties of double perovskite slab–rock salt layer $Ln_2SrAl_2O_7$ (Ln = La, Nd, Sm, Eu, Gd or Dy) natural superlattice structure. *Acta Mater* 2012, **60**: 3380–3392.

[12] Tang CC, Bando Y, Liu BD, *et al*. Cerium oxide nanotubes prepared from cerium hydroxide nanotubes. *Adv Mater* 2005, **17**: 3005–3009.

[13] Yang S, Gao L. Controlled synthesis and self-assembly of CeO_2 nanocubes. *J Am Chem Soc* 2006, **128**: 9330–9331.

[14] Lu K-Y, Ruan G-L, Ben Y-H, *et al*. Convenient synthesis of CeO_2 nanotubes. *Mat Sci Eng B* 2007, **139**: 197–200.

[15] Soren S, Bessoi M, Parhi P. A rapid microwave initiated polyol synthesis of cerium oxide nanoparticle using different cerium precursors. *Ceram Int* 2015, **41**: 8114–8118.

[16] Huang S, Feng S, Lu Q, *et al*. Cerium and niobium doped $SrCoO_{3-\delta}$ as a potential cathode for intermediate temperature solid oxide fuel cells. *J Power Sources* 2014, **251**: 357–362.

[17] Wang C, Huang W, Wang Y, *et al*. Synthesis of monodispersed $La_2Ce_2O_7$ nanocrystals via hydrothermal method: A study of crystal growth and sintering behavior. *Int J Refract Met H* 2012, **31**: 242–246.

[18] Cao X, Vassen R, Fischer W, *et al*. Lanthanum–cerium oxide as a thermal barrier coating material for high-temperature applications. *Adv Mater* 2003, **15**: 1438–1442.

[19] Patwe SJ, Amberkar BR, Tyagi AK. Synthesis, characterization and lattice thermal expansion of some compounds in the system $Gd_2Ce_xZr_{2-x}O_7$. *J Alloys Compd* 2005, **389**: 243–246.

[20] Zhang H, Li X, Gang L, *et al*. Preparation, characterization and thermophysical properties of $(Sm_{1-x}Gd_x)_2Ce_2O_7$ solid solutions. *Ceram Int* 2014, **40**: 4567–4573.

[21] Zhang H, Yan S, Chen X. Preparation and thermophysical properties of fluorite-type samarium–dysprosium–cerium oxides. *J Eur Ceram Soc* 2014, **34**: 55–61.

[22] Zha S, Xia C, Meng G. Effect of Gd (Sm) doping on properties of ceria electrolyte for solid oxide fuel cells. *J Powder Sources* 2003, **115**: 44–48.

[23] Zha S, Cheng J, Fu Q, *et al*. Cerium fuel cells based on ceria–carbonate salt composite electrolyte. *Mater Chem Phys* 2003, **77**: 594–597.

[24] Zhu B, Albinsson I, Andersson C. Electrolysis studies based on ceria-based composites. *Electrochem Commun* 2006, **8**: 495–498.

[25] Meng GY, Fu QX, Zha SW, *et al*. Novel intermediate temperature ceramic fuel cells with doped ceria-based composite electrolytes. *Solid State Ionics* 2002, **148**: 533–537.

[26] Leitner J, Chuchvalec P, Sedmidubský D, *et al*. Estimation of heat capacities of solid mixed oxides. *Thermochim Acta* 2003, **395**: 27–46.

[27] Rao KK, Banu T, Vithal M, *et al*. Preparation and characterization of bulk and nano particles of $La_2Zr_2O_7$ and $Nd_2Zr_2O_7$ by sol–gel method. *Mater Lett* 2002, **54**: 205–210.

[28] Salehi S, Fathi MH. Fabrication and characterization of sol–gel derived hyroxyapptite/zirconia composite nanopowders with various yttria content. *Ceram Int* 2010, **36**: 1659–1667.

[29] Gedanken A, Reisfeld R, Sominski E, *et al*. Sonochemical preparation and characterization of europium oxide doped in and coated on ZrO_2 and yttrium-stabilized zirconium (YSZ). *J Phys Chem B* 2000, **104**: 7057–7065.

[30] Mcdevitt NT, Baun WL. Infrared absorption study of metal oxides in the low frequency region (700–240 cm^{-1}). *Spectrochim Acta* 1964, **20**: 799–808.

[31] Arumugam A, Karthikeyan C, Hameed ASH, *et al*. Synthesis of cerium oxide nanoparticles using *Gloriosa superba* L. leaf extract and their structure, optical and antibacterial properties. *Mat Sci Eng C* 2015, **49**: 408–415.

[32] Kosacki I, Petrovsky V, Anderson HU, *et al*. Raman spectroscopy of nanocrystalline ceria and zirconia thin films. *J Am Ceram Soc* 2002, **85**: 2646–2650.

[33] Katta L, Sudarsanam P, Thrimurthulu G, *et al*. Doped nanosized ceria solid solutions for low temperature soot

oxidation: Zirconium versus lanthanum promoters. *Appl Catal B: Environ* 2010, **101**: 101–108.

[34] Deepa M, Rao PP, Radhakrishnan AN, *et al*. Pyrochlore type semiconducting ceramic oxides in Ca–Ce–Ti–M–O system (M = Nb or Ta)—Structure, microstructure and electrical properties. *Mater Res Bull* 2009, **44**: 1481–1488.

[35] Patil S, Seal S, Guo Y, *et al*. Role of trivalent La and Nd dopants in lattice distortion and oxygen vacancy generation in cerium oxide nanoparticles. *Appl Phys Lett* 2006, **88**: 243110.

[36] Deus RC, Cortés JA, Ramirez MA, *et al.* Photoluminascence properties of cerium oxide nanoparticles as a function of lanthanum content. *Mater Res Bull* 2015, **70**: 416–423.

[37] Heine V, Welche PRL, Dove MT. Geometrical origin and theory of negative thermal expansion in framework structures. *J Am Ceram Soc* 1999, **82**: 1793–1802.

[38] Lehmann H, Pitzer D, Pracht G, *et al*. Thermal conductivity and thermal expansion coefficients of the lanthanum rare earth element zirconate system. *J Am Ceram Soc* 2003, **86**: 1338–1344.

[39] Soyez G, Eastman JA, Thompson LJ, *et al*. Grain-size-dependent thermal conductivity of nanocrystalline yttria-stabilized zirconia films grown by metal-organic chemical vapor deposition. *Appl Phys Lett* 2000, **77**: 1155.

[40] Klemens PG. Phonon scattering by oxygen vacancies in ceramics. *Physica B* 1999, **263–264**: 102–104.

[41] Scheetz BE, White BW. Characterization of anion disorder in zirconate $A_2B_2O_7$ compounds by Raman spectroscopy. *J Am Ceram Soc* 1979, **62**: 468–470.